JCI insight

Cxcr3-expressing leukocytes are necessary for neurofibroma formation in mice

Jonathan S. Fletcher, … , Nathan Salomonis, Nancy Ratner

JCI Insight. 2019;4(3):e98601. https://doi.org/10.1172/jci.insight.98601.

Research Article | Inflammation | Neuroscience

Graphical abstract

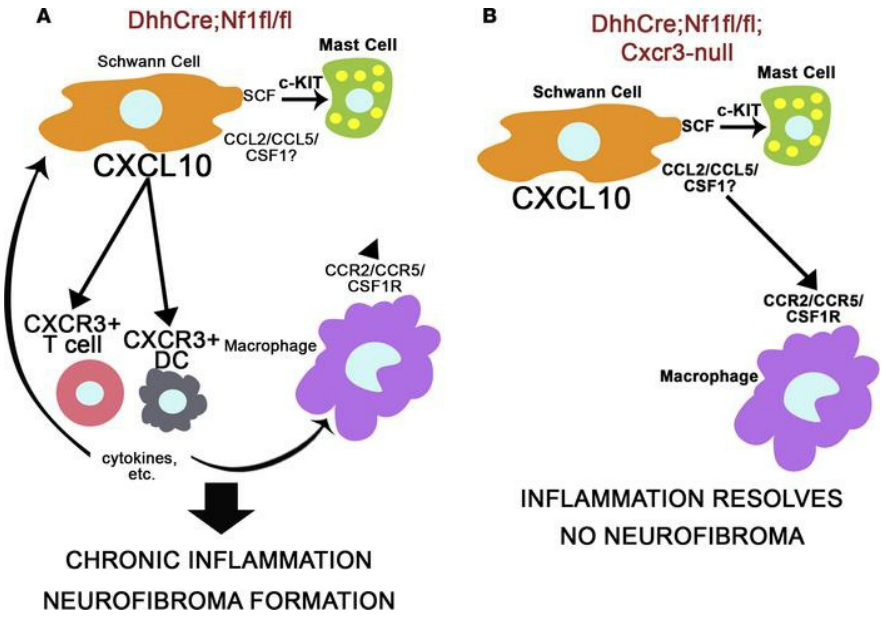

Find the latest version:

https://jci.me/98601/pdf

JCI insight

RESEARCH ARTICLE

Cxcr3-expressing leukocytes are necessary for neurofibroma formation in mice

Jonathan S. Fletcher,[1,2] Jianqiang Wu,[1] Walter J. Jessen,[1,3] Jay Pundavela,[1] Jacob A. Miller,[1] Eva Dombi,[4] Mi-Ok Kim,[5] Tilat A. Rizvi,[1] Kashish Chetal,[6] Nathan Salomonis,[6] and Nancy Ratner[1]

[1]Division of Experimental Hematology and Cancer Biology, Cincinnati Children's Hospital Medical Center, University of Cincinnati College of Medicine, Cincinnati, Ohio, USA. [2]Immunology Graduate Program, University of Cincinnati College of Medicine, Cincinnati, Ohio, USA. [3]Laboratory Corporation of America Holdings, Burlington, North Carolina, USA. [4]Center for Cancer Research, National Cancer Institute, Bethesda, Maryland, USA. [5]UCSF Helen Diller Family Comprehensive Cancer Center, Department of Epidemiology and Biostatistics, UCSF, San Francisco, California, USA. [6]Division of Biomedical Informatics, Cincinnati Children's Hospital Medical Center, University of Cincinnati College of Medicine, Cincinnati, Ohio, USA.

Plexiform neurofibroma is a major contributor to morbidity in patients with neurofibromatosis type I (NF1). Macrophages and mast cells infiltrate neurofibroma, and data from mouse models implicate these leukocytes in neurofibroma development. Antiinflammatory therapy targeting these cell populations has been suggested as a means to prevent neurofibroma development. Here, we compare gene expression in *Nf1*-mutant nerves, which invariably form neurofibroma, and show disruption of neuron–glial cell interactions and immune cell infiltration to mouse models, which rarely progresses to neurofibroma with or without disruption of neuron–glial cell interactions. We find that the chemokine Cxcl10 is uniquely upregulated in NF1 mice that invariably develop neurofibroma. Global deletion of the CXCL10 receptor Cxcr3 prevented neurofibroma development in these neurofibroma-prone mice, and an anti–Cxcr3 antibody somewhat reduced tumor numbers. *Cxcr3* expression localized to T cells and DCs in both inflamed nerves and neurofibromas, and *Cxcr3* expression was necessary to sustain elevated macrophage numbers in *Nf1*-mutant nerves. To our knowledge, these data support a heretofore-unappreciated role for T cells and DCs in neurofibroma initiation.

Introduction

Plexiform neurofibroma, a benign tumor of the Schwann cell lineage, occurs in about 50% of persons with neurofibromatosis type 1 (NF1) (1). Plexiform neurofibromas can compress neighboring vital organs and have the potential to undergo malignant transformation (1–4). Complete surgical resection of these tumors is difficult because of both their diffuse and infiltrative nature and their integration with peripheral nerves (2, 3). Because these tumors are also refractory to radiotherapy and chemotherapy, research efforts have focused on identifying cellular and molecular pathways critical for neurofibroma initiation, growth, and transformation (2, 3).

Biallelic loss of the NF1 gene in Schwann cells occurs in both NF1-associated and sporadic plexiform neurofibroma (5–7). NF1 encodes neurofibromin, a negative regulator of the Ras family of protooncogenes (8–10). Plexiform neurofibromas and NF1-null Schwann cells demonstrate increased active Ras (Ras-GTP) (11, 12) and the activation of Ras downstream pathways (13–15). Notably, NF1-null Schwann cells show increased expression of leukocyte chemoattractants, including CCL2, and stem cell factor (SCF) (16, 17). Loss of NF1 also induces cellular senescence in a subset of neurofibroma cells, which may facilitate the production of additional inflammatory mediators (18). Mast cell infiltration is a long-established feature of neurofibroma (16, 19), and macrophages constitute 25% to 35% of the cellular population of plexiform neurofibromas (20). Both mast cell–targeted and macrophage-targeted therapies have been shown to modulate the development or growth of neurofibroma in genetically engineered mouse models (GEMMs) and are postulated to be important contributors to human disease (19–22). However, these leukocytes can have context-dependent pro- and antitumorigenic effects (20, 23–25). Moreover, cells labeled by panmyeloid "macrophage" markers can include monocytes, dendritic cells (DCs), and multiple

Conflict of interest: The authors have declared that no conflict of interest exists.

Submitted: November 22, 2017
Accepted: December 20, 2018
Published: February 7, 2019

Reference information:
JCI Insight. 2019;4(3):e98601. https://doi.org/10.1172/jci.insight.98601.

macrophage subpopulations with distinct activities (24, 25). Further characterization of these neurofibroma leukocytes and their contributions to tumor initiation and growth is necessary for the development of safe and effective immunomodulatory therapies.

In the *Dhh*-Cre $Nf1^{fl/fl}$ mouse neurofibroma model, biallelic deletion of *Nf1* in the Schwann cell lineage mimics the biallelic loss of *NF1* in human NF1 and sporadic plexiform neurofibroma (26). The peripheral nerves of these mice appear normal at 1 month of age, but pathological changes, including mast cell and macrophage infiltration and abnormal Schwann cell proliferation, are evident at 2 months of age (26, 27). By 4 months of age, these mice invariably form MRI-detectable paraspinal neurofibromas that histologically and transcriptionally resemble human plexiform neurofibroma (26, 28, 29). Schwann cell–specific deletion of *Nf1* using other drivers can also induce nerve pathology and neurofibroma development in mice (19, 30–32). In contrast, *CNPase*–human EGFR (*CNPase*-hEGFR) mice have increased Ras activity driven by overexpression of hEGFR and develop similar nerve pathology to *Nf1* mouse models but have reduced myeloid cell infiltration, and only approximately 1 in 20 develop a neurofibroma (20, 33).

Here, we compare nerves from these mouse models transcriptionally and identify a chemokine, *Cxcl10*, that is uniquely overexpressed in 2-month *Dhh*-Cre $Nf1^{fl/fl}$ nerves. CXCL10 and its receptor, CXCR3, are important modulators of neuroinflammation and tumor biology (34–36). In this study, we identify *Cxcl10*- and *Cxcr3*-expressing cell populations in nerves and neurofibroma and demonstrate the necessity of *Cxcr3* for neurofibroma development in *Dhh*-Cre $Nf1^{fl/fl}$ mice.

Results

Differential gene expression analyses identify Cxcl10 as a potential modulator of plexiform neurofibroma development. Peripheral nerves from GEMMs of NF1 (GEMM-NF1) (*P0*-CreB $Nf1^{fl/fl}$, *P0*-CreB $Nf1^{fl/-}$, *Dhh*-Cre $Nf1^{fl/fl}$) invariably develop neurofibromas (26, 31). *P0*-CreB and *Dhh*-Cre are transgenic mouse strains that express Cre recombinase in peripheral nerve Schwann cells; when used to recombine *Nf1* in mice, peripheral nerves show pathological mast cell recruitment, disruption of axon and nonmyelinating Schwann cell (axon/Remak bundle) interactions, and collagen deposition (nerve disruption). This nerve disruption phenotype precedes plexiform neurofibroma development. Although several of these changes have been proposed to contribute to neurofibroma development, similar nerve pathology is also observed in *CNPase*-hEGFR/$^{+}$ and *CNPase*-hEGFR/*CNPase*-hEGFR mice, which recruit fewer macrophages and rarely form neurofibromas (33, 37). In contrast, this pathology is not observed in Npcis mice ($Nf1^{+/-}$ $Trp53^{+/-}$ deletions in *cis*) that progress directly to malignant peripheral nerve sheath tumor (ref. 38 and Supplemental Figure 1; supplemental material available online with this article; https://doi.org/10.1172/jci.insight.98601DS1) or in *CNPase*-HRas12V mice that do not develop plexiform neurofibroma (39). We hypothesized that GEMMs with this common pattern of GEMM-NF1–associated nerve pathology would also share common gene expression programs or have similar transcriptional profiles. To test this, we compared gene expression patterns between adult sciatic nerves from the models with GEMM-NF1–associated nerve pathology (*P0*-CreB $Nf1^{fl/fl}$ [n = 4], *P0*-CreB $Nf1^{fl/-}$ [n = 4], *Dhh*-Cre $Nf1^{fl/fl}$ [n = 5], *CNPase*-hEGFR/$^{+}$ [n = 4], and *CNPase*-hEGFR/*CNPase*-hEGFR [n = 4]) and those without (Npcis [n = 4] and CNP-HRas12V [n = 6]) with normal control nerves from these mouse lines ($Nf1^{fl/fl}$, *P0*-Cre, and $Nf2^{fl/fl}$ [n = 11]). We identified 2,028 transcripts significantly differentially expressed across samples (ANOVA, $P < 0.05$, Benjamini-Hochberg FDR). Differentially expressed genes were partitioned into 6 K-means clusters, C1–C6. Gene expression clusters C1 and C6 were similarly expressed across disrupted GEMM-NF1 nerves (Figure 1A), distinct from undisrupted nerves, as compared with WT adult sciatic nerves. GO terms ($P < 0.05$) associated with cluster C6 (upregulated in disrupted nerve) included chemotaxis, angiogenesis, extracellular matrix organization and biogenesis, Wnt signaling, cell differentiation, and EGFR signaling, consistent with nerve disruption phenotypes. The gene expression in these clusters was highly similar between disrupted *Dhh*-Cre $Nf1^{fl/fl}$ and *CNPase*-hEGFR nerves, despite the disparate outcomes in these models.

Myelination and Remak bundle formation is largely complete by 1 month of age in mice, whereas mast cell and macrophage recruitment in *Dhh*-Cre $Nf1^{fl/fl}$ and *CNPase*-hEGFR nerves begins between 1 and 2 months of age (20, 34). To distinguish transcriptional changes associated with nerve disruption or inflammation from those associated with nerve maturation, we analyzed gene expression in 1- and 2-month-old nerves from *Dhh*-Cre $Nf1^{fl/fl}$ and *CNPase*-hEGFR nerves and age-matched, WT control nerves ($Nf1^{fl/fl}$). No changes were identified among the 3 groups at 1 month of age (Figure 1B; 4-week-old nerve). At 8 weeks of age, expression of genes from clusters C1 and C6 (Figure 1A) associated with nerve disruption in the prior analysis (indicated in green at the right

of the heatmap), was similarly upregulated or downregulated in 2-month *Dhh*-Cre *Nf1*$^{fl/fl}$ and *CNPase*-hEGFR nerves and was distinct from 2-month controls (*Nf1*$^{fl/fl}$) and 1-month-old nerves of all 3 genotypes: *Nf1*$^{fl/fl}$ (WT), EGFR/EGFR, or *Dhh*-Cre *Nf1*$^{fl/fl}$) (Figure 1B). This supports the hypothesis that the gene expression changes in GEMM nerves are related to the nerve disruption phenotype and not to altered nerve maturation.

Despite the phenotypic and transcriptional similarities of their initial nerve pathology, the *Dhh*-Cre *Nf1*$^{fl/fl}$ and *CNPase*-hEGFR/*CNPase*-hEGFR mouse models diverged significantly in their rates of neurofibroma formation. We hypothesized that genes showing maximal differential expression between *Dhh*-Cre *Nf1*$^{fl/fl}$ and *CNPase*-hEGFR nerves would be enriched for modulators of tumorigenesis. Only 38 genes were greater than 2-fold upregulated or downregulated in *Dhh*-Cre *Nf1*$^{fl/fl}$ but not *CNPase*-hEGFR nerves relative to their 2-month control nerves; the 7 most upregulated genes are shown in Figure 1C.

Among the genes uniquely upregulated in 2-month *Dhh*-Cre *Nf1*$^{fl/fl}$ nerves, *Cxcl10* was the only differentially expressed cytokine (Figure 1C). Because CXCL10 signaling through its receptor, CXCR3, can have important roles in neuroinflammatory processes and tumor biology (34–36), we identified this pathway as a candidate for further study.

We used quantitative PCR to verify that *Cxcl10* is overexpressed in 2-month *Dhh*-Cre *Nf1*$^{fl/fl}$ nerve/dorsal root ganglia (DRG) (>4-fold) and is further increased (~16-fold) in GEMM-NF1 from these mice (Figure 1D). *Cxcr3* expression was also increased in neurofibroma, consistent with a role for *Cxcr3*-expressing cells in tumor development (Figure 1E). Thus, *Cxcr3* is low at the 2-month time point and is increased in neurofibroma, at 7 months. The expression of the alternative CXCR3 ligands, *Cxcl9* and *Cxcl11*, was also increased in neurofibroma but not in 2-month DRG (Figure 1, F and G).

Cxcl10 expression is correlated with Schwann cell–associated gene expression in single cells. We first attempted to locate CXCL10 in nerve/DRG by immunostaining. Anti–CXCL10 antibodies were specific in positive controls: pancreatic islets expressing CXCL10 under the rat insulin promoter (40). However, these antibodies stained myelin in both experimental nerve/DRG and *Cxcl10*-null negative controls (not shown). Therefore, to identify cell populations associated with *Cxcl10* expression, we used a single-cell RNA Sequencing (scRNA-Seq) data set collected from 2-month *Dhh*-Cre *Nf1*$^{fl/fl}$ nerve/DRG using the 10x Genomics Chromium platform. Analysis of the associated 1,820 cell barcode profiles identified 8 distinct cell clusters (C1–C7 and C9, Figure 2A). One preliminary cluster, C8, was excluded following multiplet exclusion because it did not contain a distinct pattern of population-specific gene expression. On the basis of their population-specific gene expression patterns, these clusters were tentatively identified as specific cellular populations (C1: monocyte/macrophage, C2–C6: neurons, C7 and C9: Schwann cells). The cell cluster C7 included cells expressing genes associated with nonmyelinating Schwann cells (SCs) and SCs that have lost contact with axons (e.g., *Gap43*, *Ngfr*, *Bdnf*, and *Stmn1*). Cells in cell cluster C9 expressed markers of myelinating SCs (e.g., *Plp1*, *Qk*, and *Vim*) but cells that expressed the immature SC marker *Fabp7* (*Blbp*). *Cxcr3* was not detected in any cells in this analysis of 2-month-old mice. Next, we examined expression of *Cxcl10* in these clusters. As visualized by t-distributed stochastic neighbor embedding (t-SNE) plots, *Cxcl10* expression localizes to cell cluster C9 (labeled SC-2) (Figure 2B). To further explore *Nf1* and *Cxcl10* expression, we plotted their relative expression in individual cells in SC-1 (C7) and SC-2 (C9) (Figure 2C). Although 26.2% of cells in SC-2 retained *Nf1* expression and expressed *Cxcl10* (red dots within box in Figure 2C), in general, *Nf1* is expressed in cells in SC-1 (blue dots along *y* axis); most *Cxcl10*-expressing cells in SC-2 (red dots along *x* axis) have low or undetectable *Nf1*.

To better phenotype *Cxcl10*-expressing cells in SC-2, we performed an independent unsupervised analysis (Figure 2D). Consistent with the t-SNE visualization, independent subsets of SC clusters were obtained from this analysis; cells polarized to either *Fabp7*^{hi} or *Cxcl10*^{hi} expression. In SC-2, subcluster 1 contained a *Cxcl10*-expressing but relatively *Cxcl10*^{lo} cell population associated with higher expression of satellite glial cell/SC precursor markers (*Fabp7*/*Blbp*, *Apoe*, *Hes5*, *Plp1*). In SC-2, subcluster 3, *Cxcl10*-expressing but relatively *Cxcl10*^{hi} cells were enriched for transcriptional readouts of Ras pathway activation (*Fos*, *Junb*, *Atf4*) and regulators of stress/apoptosis, such as *Cdkn2*, *Gadd45a*, *Nfkbia*, and *Id3* (Supplemental Table 2). Together, these data suggest that *Cxcl10* is produced by a subset of satellite cells or immature, possibly dedifferentiated, SCs in 2-month *Dhh*-Cre *Nf1*$^{fl/fl}$ DRG and that *Cxcl10* expression is correlated with activated Ras/MEK/ERK signaling in these cells. Next, we further explored the importance of CXCL10/CXCR3 signaling in plexiform neurofibroma development. Given the expression of all 3 canonical CXCR3 ligands in neurofibroma and the possibility of ligand redundancy in neurofibroma development, we targeted the CXCL10 receptor, CXCR3, in these functional studies (41).

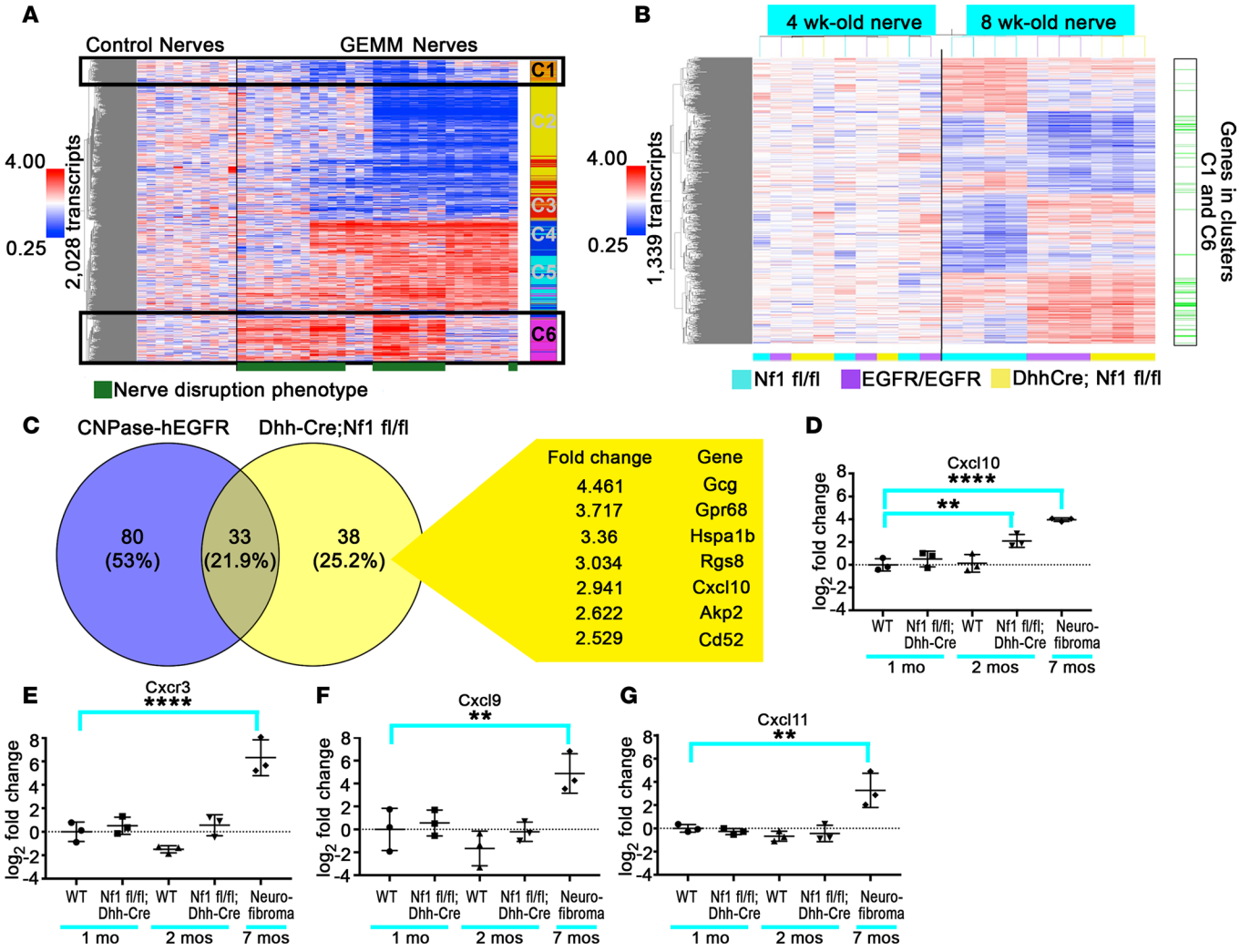

Figure 1. Gene expression reveals differential expression of *Cxcl10* in neurofibroma development. (**A**) Gene expression in control nerves compared with *Nf1*-mutant GEMM and related EGFR and HRas mouse models; 2,028 genes were differentially expressed (ANOVA, $P < 0.05$, Benjamini-Hochberg FDR), forming 6 distinct gene expression clusters. Relative levels of gene expression are shown as fold change (left); red means high and blue means low gene expression. Clusters were refined using K-means clustering ($n = 6$) for subsequent gene ontology (GO) analyses (the colored column to the right of the heatmap labeled C1–C6 represents K-means clusters). The pattern of gene expression in clusters C1 and C6 was associated with the presence of nerve disruption, a common pattern of axon-glial dissociation, fibrosis, and inflammation occurring in plexiform neurofibroma mouse models and *CNPase*-hEGFR nerves, which is designated by a green bar under the heatmap. (**B**) An independent analysis of 1-month and 2-month $Nf1^{fl/fl}$ (control), *CNPase*-hEGFR/ *CNPase*-hEGFR, and *Dhh*-Cre $Nf1^{fl/fl}$ nerves identified 1,339 genes as differentially expressed between these groups at the 2-month but not the 1-month time point (ANOVA, $P < 0.05$, Benjamini-Hochberg FDR; $n = 4$ for the 2-month $Nf1^{fl/fl}$ control, $n = 3$ other groups). *CNPase*-hEGFR/*CNPase*-hEGFR and *Dhh*-Cre $Nf1^{fl/fl}$ nerves at the 2-month time point shared a common pattern of gene regulation distinct from maturation-associated changes in 2-month controls. Consistent with the presence of the nerve disruption phenotype in these 2-month experimental nerves, many of these differentially expressed genes were associated with the nerve disruption phenotype identified in **A** (indicated by the column to the right of the heatmap in **B**). (**C**) Genes differentially expressed between *Dhh*-Cre $Nf1^{fl/fl}$ and *CNPase*-hEGFR/*CNPase*-hEGFR nerve/DRG. Only 38 genes were significantly upregulated or downregulated greater than 2-fold in 2-month *Dhh*-Cre $Nf1^{fl/fl}$ nerve/DRG relative to 2-month $Nf1^{fl/fl}$ controls that were not similarly upregulated or downregulated in *CNPase*-hEGFR/*CNPase*-hEGFR nerve/DRG ($P < 0.05$, Benjamini-Hochberg FDR) in *Dhh*-Cre $Nf1^{fl/fl}$ nerve/DRG but not CNPase-hEGFR nerve/DRG (relative to their respective controls). The 7 most upregulated genes are shown. *Cxcl10* was the only cytokine uniquely upregulated in *Dhh*-Cre $Nf1^{fl/fl}$ nerve/DRG. (**D**) *Cxcl10* upregulation in 2-month *Dhh*-Cre $Nf1^{fl/fl}$ ($n = 3$ all groups) nerve/DRG was validated by quantitative PCR (**$P < 0.01$, Dunnett's multiple-comparisons test [MCT]). *Cxcl10* was also upregulated in neurofibroma (****$P < 0.0001$, Dunnett's MCT). (**E–G**) Its receptor, *Cxcr3* (****$P < 0.0001$, Dunnett's MCT), and its alternative ligands, *Cxcl9* and *Cxcl11* (**$P < 0.01$, Dunnett's MCT), were overexpressed in neurofibroma but not in 2-month *Dhh*-Cre $Nf1^{fl/fl}$ nerve/DRG ($n = 3$ all groups). Symbols represent individual mice; horizontal bars indicate the mean ± SD.

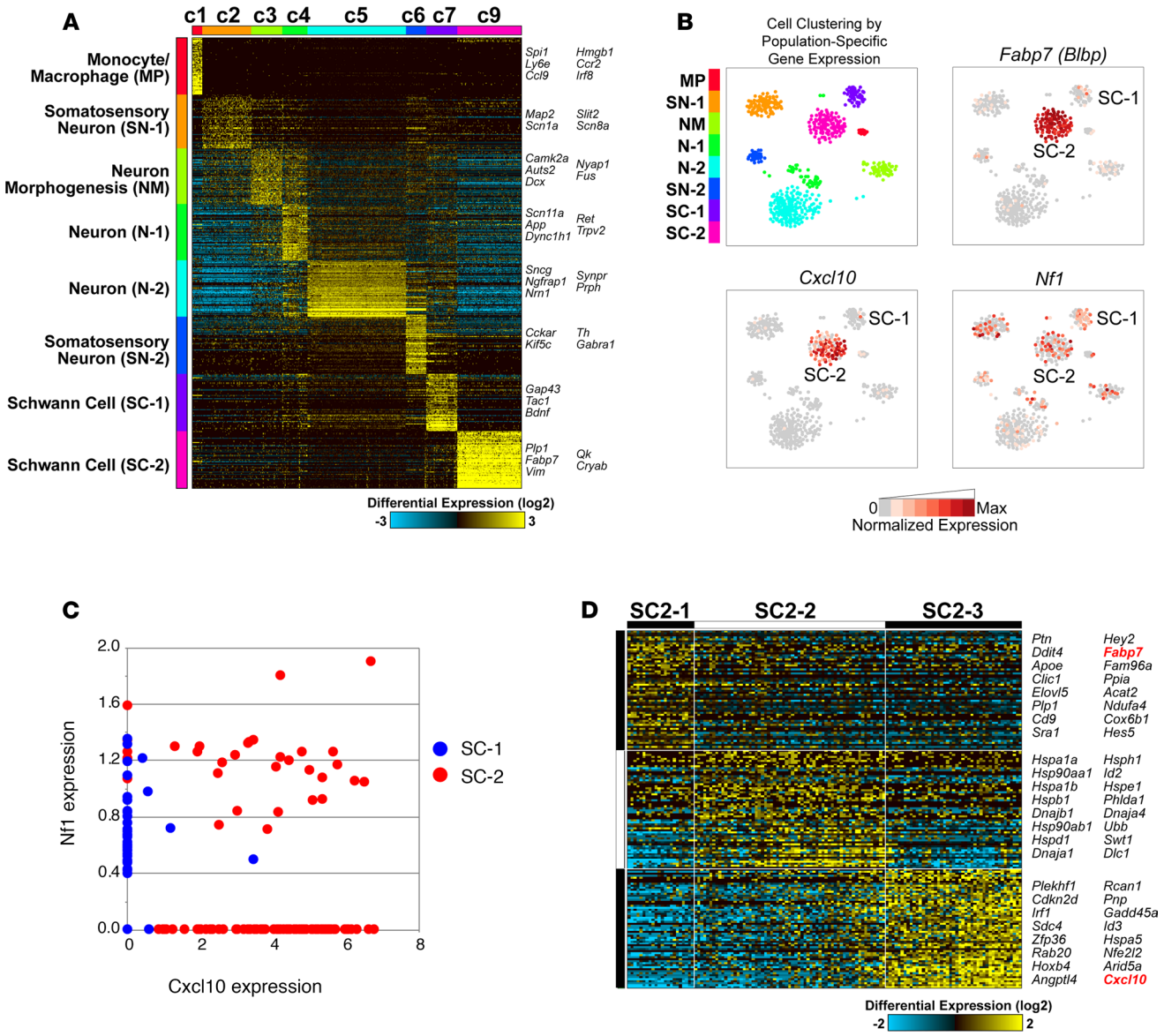

Figure 2. *Cxcl10* and associated gene expression in single-cell sequencing from 2-month *Dhh*-Cre *Nf1*$^{fl/fl}$ nerve/DRG. (**A**) Iterative Clustering and Guide-gene Selection (ICGS) performed with the MarkerFinder analysis option initially identified 9 primary cell populations and associated population-specific genes. Results are shown following multiplet cell and cluster (C8) exclusion. The cell types of these clusters were then inferred on the basis of their associated population-specific genes relative to published references and the GO. (**B**) Visualization of cell populations by t-SNE (arbitrary units). *Fabp7* (*Blbp*), an immature SC marker gene, is localized to SC cluster C9 (SC-2). *Cxcl10* is also predominantly localized to this cluster. The pattern of *Nf1* localization is different from that of *Cxcl10*. (**C**) Single cells in SC-1 (blue dots) and SC-2 (red dots), plotted by normalized expression of *Cxcl10* and *Nf1*. *Nf1*-expressing cells in SC-1 largely lack *Cxcl10* and are compressed on the *y* axis, while 73.8% of *Cxcl10*-expressing cells in SC-2 lack *Nf1* expression and are compressed on the *x* axis. (**D**) Unsupervised analysis of SCs in cluster C9 by ICGS partitions these cells into 3 subclusters, distinguished by localization of *Fabp7* (cluster C1) and *Cxcl10* (cluster C3).

Cxcr3 deletion prevents GEMM-NF1 development and reduced nerve pathology in mice. To test the importance of CXCR3 signaling in neurofibroma development, we generated *Dhh*-Cre *Nf1*$^{fl/fl}$ *Cxcr3*-null mice. *Dhh*-Cre *Nf1*$^{fl/fl}$ *Cxcr3*-null mice survived significantly longer than *Dhh*-Cre *Nf1*$^{fl/fl}$ controls (Figure 3A). *Dhh*-Cre *Nf1*$^{fl/fl}$ survival mice were predominantly sacrificed due to neurofibroma-associated morbidity (e.g., paralysis), while sacrifice of *Dhh*-Cre *Nf1*$^{fl/fl}$ *Cxcr3*-null mice was typically necessitated by dermatitis (n = 3 mice) and abdominal bloating/lethargy associated with malignancies typical of aged C57/Bl6 mice (n = 5 colon and hepatic tumors). Thirteen *Dhh*-Cre *Nf1*$^{fl/fl}$ *Cxcr3*-null mice were collected at 18 to 20 months with thorough dissection of the spinal cord/DRG and tissue collection for analysis. No paraspinal neurofibromas were present in *Dhh*-Cre *Nf1*$^{fl/fl}$ *Cxcr3*-null mice from the survival cohort. In contrast, all mice in the *Dhh*-Cre *Nf1*$^{fl/fl}$ group developed multiple paraspinal neurofibromas.

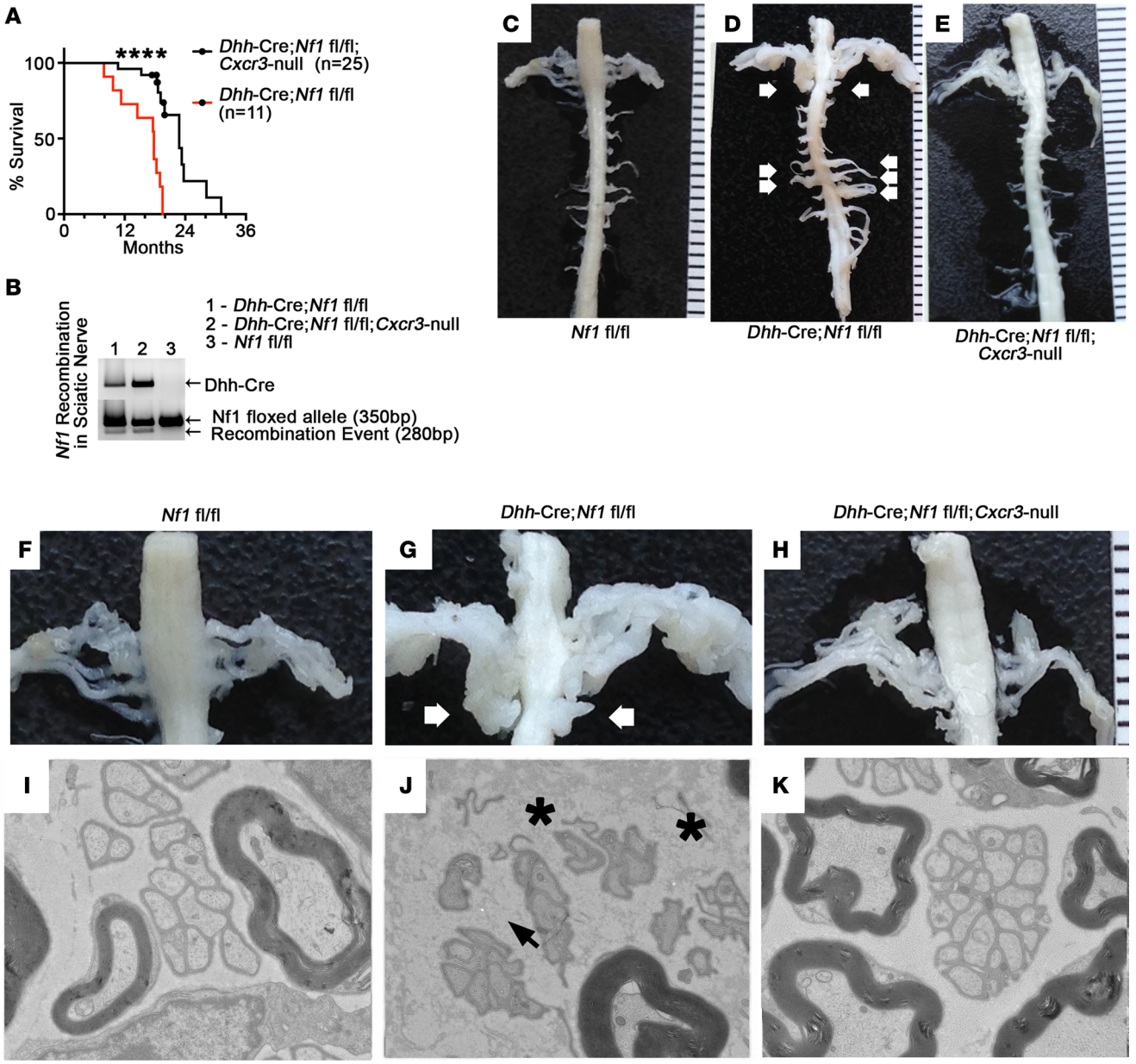

Figure 3. Global deletion of *Cxcr3* prevents plexiform neurofibroma and reduces nerve pathology in *Dhh*-Cre *Nf1*$^{fl/fl}$ mice. (**A**) *Dhh*-Cre *Nf1*$^{fl/fl}$ *Cxcr3*-null (n = 25) mice survived significantly longer than *Dhh*-Cre *Nf1*$^{fl/fl}$ (n = 11) mice (****P < 0.0001, log-rank test). All of the *Dhh*-Cre *Nf1*$^{fl/fl}$ and none of the *Dhh*-Cre *Nf1*$^{fl/fl}$ *Cxcr3*-null mice developed neurofibromas. Censored data points represent *Dhh*-Cre *Nf1*$^{fl/fl}$ *Cxcr3*-null mice collected at 18 to 20 months of age for dissection, pathological analyses, and histological analyses. (**B**) Loss of *Cxcr3* did not prevent *Nf1* recombination in *Dhh*-Cre *Nf1*$^{fl/fl}$ *Cxcr3*-null sciatic nerve. (**C**–**E**) Representative images of age-matched (10-month) spinal cords and associated spinal nerve/DRG are shown; such dissections were performed on all study mice (n > 10 each group). White arrows indicate plexiform neurofibromas. (**F**–**H**) Close-up of **C**–**E**; white arrows indicate bilateral plexiform neurofibromas compressing the spinal cord. (**I**–**K**) Representative electron micrographs from saphenous nerves (n = 3 examined for each genotype). (**I**) Electron micrograph of a normal 7-month saphenous nerve. (**J**) Black arrowhead indicates a disrupted Remak bundle in *Dhh*-Cre *Nf1*$^{fl/fl}$ saphenous nerve. Dark gray particulate (black asterisks) indicates deposited collagen. (**K**) Remak bundle disruption and collagen deposition were absent in 7-month *Dhh*-Cre *Nf1*$^{fl/fl}$ *Cxcr3*-null saphenous nerves. Original magnification, 4000× (**I**, **J**, and **K**).

Absence of neurofibromas in *Dhh*-Cre *Nf1*$^{fl/fl}$ *Cxcr3*-null mice was not the result of a lack of *Nf1* recombination in the nerves of *Dhh*-Cre *Nf1*$^{fl/fl}$ *Cxcr3*-null mice (Figure 3B). Representative, age-matched spinal cord dissections demonstrated the absence of plexiform neurofibroma and associated spinal nerve hypertrophy in *Dhh*-Cre *Nf1*$^{fl/fl}$ *Cxcr3*-null animals (Figure 3, C–H).

Because *Dhh*-Cre *Nf1*$^{fl/fl}$ *Cxcr3*-null mice did not exhibit generalized peripheral nerve hypertrophy, we collected additional mice for electron microscopy to examine the effects of *Cxcr3* deletion on the nerve

disruption phenotype. Surprisingly, neither axon-glial dissociation nor collagen deposition were evident in 7-month *Dhh*-Cre *Nf1*$^{fl/fl}$ *Cxcr3*-null peripheral nerves (Figure 3, I–K). Although fibrosis in neurofibroma was evident by trichrome staining, the more subtle collagen deposition phenotype in nerves was less evident (Supplemental Figure 2A).

Cxcr3 deletion does not prevent mast cell recruitment but resulted in a delayed resolution of macrophage infiltration. Mast cell activity has been postulated to mediate GEMM-NF1–associated nerve pathology and to contribute to plexiform neurofibroma development. Therefore, we examined whether the recruitment of mast cells, which have been reported to express CXCR3 (42, 43), is reduced in *Dhh*-Cre *Nf1*$^{fl/fl}$ *Cxcr3*-null mice. Because *Dhh*-Cre *Nf1*$^{fl/fl}$ *Cxcr3*-null mice did not develop neurofibroma, we quantified these cells in 2-month and 7-month sciatic nerve sections by toluidine blue staining (Figure 4A). A trend toward fewer mast cells was observed in *Dhh*-Cre *Nf1*$^{fl/fl}$ *Cxcr3*-null nerves, but this trend did not reach significance at either time point (Figure 4B). Similar results were observed when identifying mast cells by Leder stain (Supplemental Figure 2, B and C). We also quantified macrophages, which likewise accumulate in disrupted nerves and neurofibroma, by Iba-1$^+$ expressivity (Figure 4, C and D). Interestingly, loss of *Cxcr3* did not prevent the initial recruitment of these cells to *Dhh*-Cre *Nf1*$^{fl/fl}$ *Cxcr3*-null nerves observed at 2 months but resulted in the resolution of macrophage infiltration by 7 months (Figure 4, C and D).

To determine whether the reduction in macrophages seen at 7 months is directly mediated by CXCR3 expression on macrophages, we crossed *Dhh*-Cre *Nf1*$^{fl/fl}$ mice to the *Cxcr3* internal ribosomal entry site bicistronic EGFP reporter (CIBER) mouse line (44). CIBER mice express WT CXCR3 at physiological levels and coexpress EGFP in cells from the transgenic *Cxcr3* mRNA (44). In 2-month *Dhh*-Cre *Nf1*$^{fl/fl}$ CIBER nerve/DRG, *Cxcr3*-expressing cells were present but did not colocalize with the macrophage marker Iba-1 (Figure 4E) or 2 other macrophage markers (CD11b or F4/80, Supplemental Figure 3, A and B). However, all *Cxcr3*-expressing cells in these nerves/DRG were CD45$^+$ (Figure 4F), consistent with a hematopoietic origin.

Cxcr3-expressing T cells and DCs are present in Dhh-Cre Nf1$^{fl/fl}$ *CIBER nerve/DRG and neurofibroma*. Because *Cxcr3*-expressing cells were CD45$^+$, we tested the colocalization of *Cxcr3* expression with other leukocyte markers. In both 2-month *Dhh*-Cre *Nf1*$^{fl/fl}$ CIBER mice (Figure 5A) and 7-month neurofibromas (Figure 5B), *Cxcr3* expression frequently colocalized to T cells (CD3$^+$) and DCs (CD11c$^+$). Both CD4$^+$ and CD8$^+$ T cells expressed *Cxcr3* in neurofibroma (Supplemental Figure 4, C and D). In contrast, *Cxcr3*-expressing cells were largely absent from WT, 2-month nerve/DRG. Of the *Cxcr3*-expressing cells present in disrupted nerve/DRG and neurofibroma, more than 95% of these cells were either T cells or DCs (Figure 5C). Interestingly, foci of *Cxcr3*-expressing T cells and DCs were frequently observed in paraspinal neurofibroma (Supplemental Figure 4A). T cells and DCs were rare in *Dhh*-Cre *Nf1*$^{fl/fl}$ distal sciatic nerves that do not develop neurofibroma in the same mice, but loss of *Cxcr3* also reduced T cells in the sciatic nerves (Figure 5D). Loss of *Cxcr3* did not significantly affect DC numbers in sciatic nerves, but only approximately 65% of DCs expressed *Cxcr3* in nerves/neurofibromas (in contrast with more than 90% of T cells), suggesting that a subpopulation of DCs may be recruited to nerves/neurofibromas in a CXCR3-independent fashion (Figure 5E and Supplemental Figure 4B). Importantly, CD3$^+$ T cells and CD11c$^+$ "DCs" were present in human plexiform neurofibroma (Figure 5, F–I), suggesting that these populations are relevant to human disease. Testing whether *CXCL10* expression is elevated early in human plexiform neurofibroma formation will require human samples not currently available. Consistent with CXCR3 expression by T cells or DCs in human tumors, *CXCR3* mRNA was elevated in human plexiform neurofibroma samples versus normal human nerves, although the difference between groups in a gene expression microarray did not reach significance in this limited sample set ($P = 0.062$) (Figure 5J).

Administration of CXCR3-neutralizing antibody CXCR3-173 does not prevent neurofibroma development or reduce the growth of established tumors. Having determined that *Cxcr3* is both present on T cells and DCs in neurofibroma and important for neurofibroma development, we next tested the effect of CXCR3 blockade on neurofibroma growth and T cell and DC composition in *Dhh*-Cre *Nf1*$^{fl/fl}$ mice. We established baseline neurofibroma size and growth kinetics by volumetric MRI, then performed follow-up imaging and histological analyses after 2 months of treatment with CXCR3-173 (Supplemental Figure 5A), an established CXCR3-neutralizing antibody (45, 46). CXCR3-173 did not reduce neurofibroma volume relative to control IgG (Supplemental Figure 5B), and blockade of CXCR3 also failed to deplete T cells or DCs in these tumors (Supplemental Figure 5, C and D).

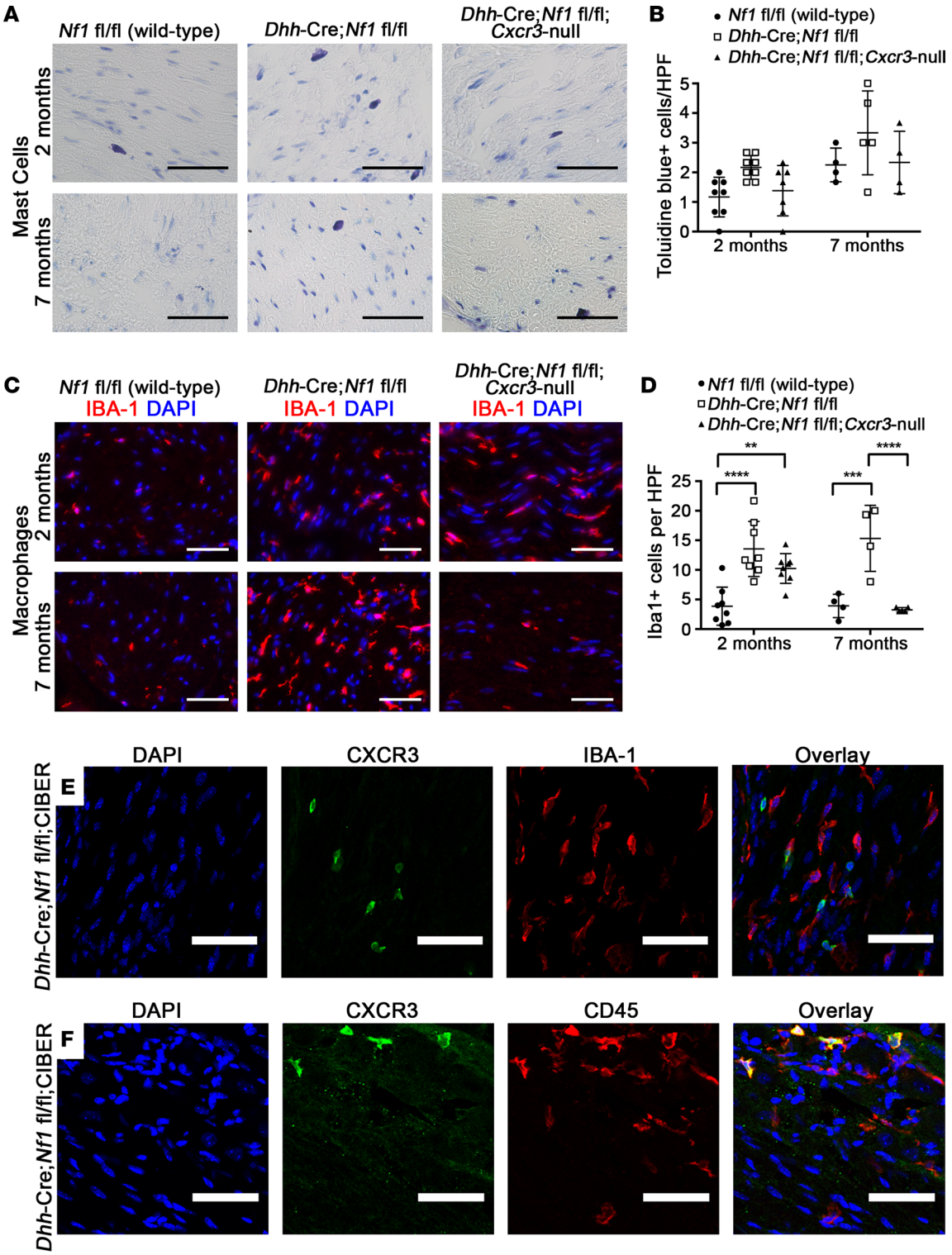

Figure 4. The effects of *Cxcr3* deletion on mast cell and macrophage infiltration of *Dhh*-Cre *Nf1*$^{fl/fl}$ nerves ($n \geq 4$ all groups). (**A**) Toluidine blue staining in 2-month and 7-month sciatic nerves (original magnification, ×40. Scale bar: 50 μm). (**B**) Mast cell infiltration of nerves was not significantly affected by loss of *Cxcr3* (NS, 2-way ANOVA). HPF, high-power field. (**C**) Iba-1 (macrophage) staining in sciatic nerves (original magnification, ×40. Scale bar: 50 μm). (**D**) Loss of *Cxcr3* did not affect the initial recruitment of macrophages to nerves but resulted in the resolution of macrophage inflammation by 7 months (**$P < 0.01$, ***$P < 0.001$, ****$P < 0.0001$, 2-way ANOVA with Tukey's MCT). Symbols represent individual mice; horizontal bars indicate the mean ± SD. (**E**) *Cxcr3* expression does not colocalize to IBA-1$^+$ macrophages (original magnification, ×20. Scale bar: 50 μm), but (**F**) *Cxcr3*-expressing cells are CD45$^+$ hematopoietic cells (original magnification, ×20. Scale bar: 50 μm).

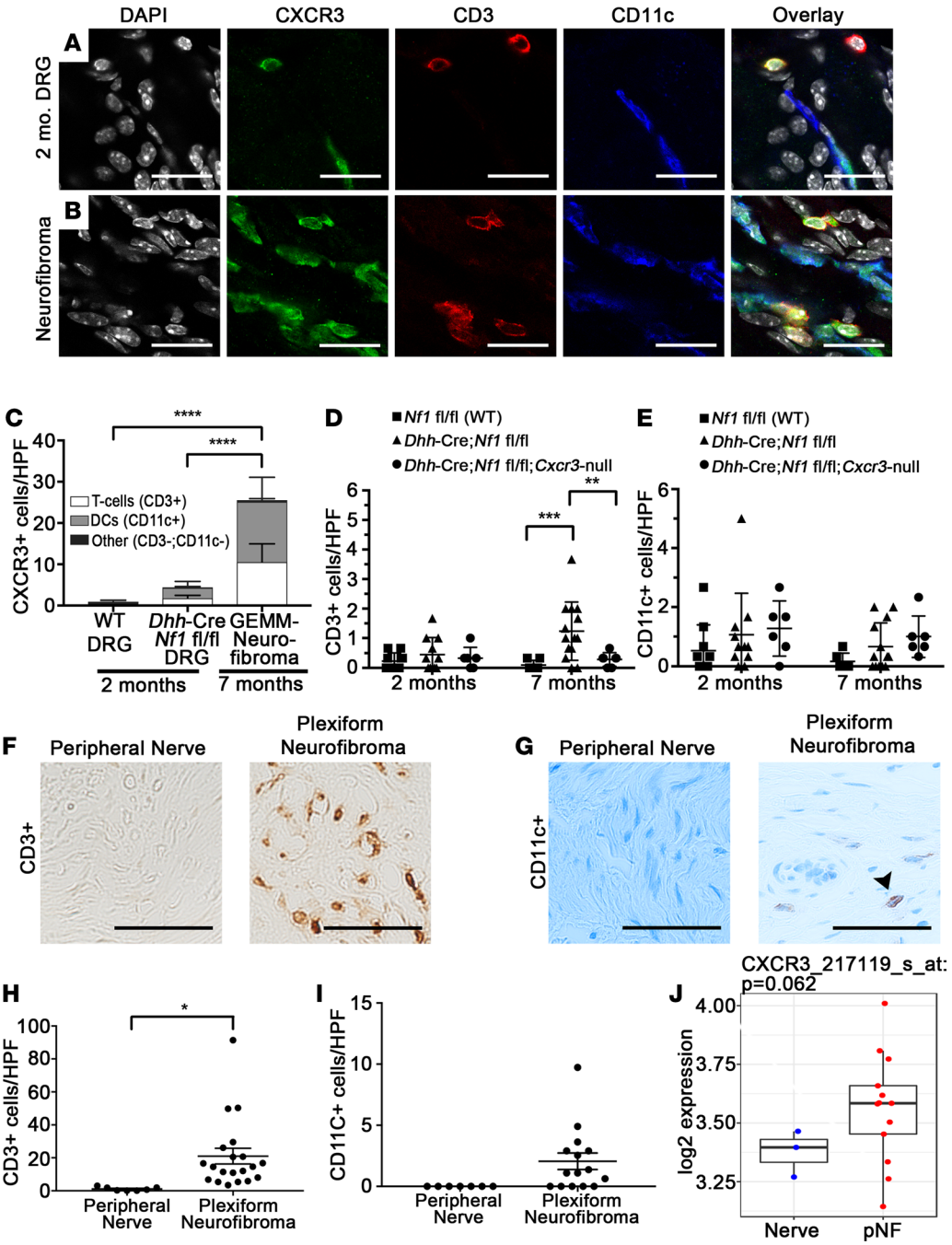

Figure 5. Identification of *Cxcr3*-expressing cells in *Dhh*-Cre *Nf1*$^{fl/fl}$ nerve/DRG and neurofibroma. (**A**) *Cxcr3* expression colocalizes with CD3$^+$ T cells and CD11c$^+$ DCs in 2-month nerve/DRG (original magnification, ×60. Scale bar: 20 μm) and (**B**) in 7-month neurofibroma (original magnification, ×60. Scale bar: 20 μm). (**C**) *Cxcr3*-expressing cells are rare in WT nerves (n = 4) and are predominantly T cells and DCs in *Dhh*-Cre *Nf1*$^{fl/fl}$ nerve/DRG (n = 9) and neurofibroma (n = 7) (****P < 0.0001, 2-way ANOVA with Tukey's MCT). The box plot depicts the minimum and maximum values (whiskers), the upper and lower quartiles, and the median. The length of the box represents the interquartile range. (**D**) T cells were rare in 2-month (n ≥ 4 all groups) sciatic nerves, but loss of *Cxcr3* reduced T cell accumulation in 7-month *Dhh*-Cre *Nf1*$^{fl/fl}$ sciatic nerves (**P < 0.01, ***P < 0.001, 2-way ANOVA with Tukey's MCT). Symbols represent individual mice; horizontal bars indicate the mean ± SD. (**E**) DC numbers in sciatic nerves were unaffected by loss of *Cxcr3* (NS, 2-way ANOVA). (**F** and **G**) Colorimetric (DAB) staining of CD3$^+$ T cells and CD11c$^+$ DCs in human peripheral nerve and plexiform neurofibroma (original magnification, ×40. Scale bar: 50 μm). (**F**) T cells are absent in normal human peripheral nerves (n = 7) but numerous in human plexiform neurofibroma (n = 19). (**G**) DCs are absent in human peripheral nerves (n = 7) but detectable in some human plexiform neurofibromas (n = 15). Arrowhead points to CD11c$^+$ (brown) cell. (**H**) Quantification of T cells (*P < 0.01, unpaired t test) and (**I**) quantification of CD11c$^+$ cells (NS, P = 0.056, unpaired t test) in human tissue sections. (**J**) Box-and-whisker plot showing relative *CXCR3* mRNA expression in human plexiform neurofibroma (pNF) versus normal human nerve. The box plot depicts the minimum and maximum values (whiskers), the upper and lower quartiles, and the median. The length of the box represents the interquartile range.

The failure of CXCR3 blockade in treating neurofibroma suggested that there might be a critical window in which CXCR3 signaling contributes to the development of this disease. Therefore, we designed a preventative trial to determine whether CXCR3-173 can inhibit neurofibroma development in *Dhh*-Cre *Nf1*$^{fl/fl}$ mice. Mice were administered CXCR3-173 from either 1 week or 1 month of age, before significant increases in numbers of leukocytes, to 4 months of age, when untreated mice invariably develop neurofibroma (Supplemental Figure 5E). The number of CD3$^+$ T cells in neurofibromas was also not reduced by CXCR3-173 treatment (Supplemental Figure 5G), although CD11c$^+$ DCs were modestly reduced in CXCR3-173–treated animals (Supplemental Figure 5H). Mice treated beginning at 1 week of age with CXCR3-173 did not show significantly altered tumor burden on MRI examination at 4 months of age (Supplemental Figure 5F). Gross dissection of the neuroaxis in mice treated beginning at 1 week of age with CXCR3-173 confirmed that tumor size was not changed (Supplemental Figure 5F), with overall tumor volumes in both IgG control– and CXCR3-173–treated mice consistent with historical controls (not shown and Supplemental Figure 5, J and K). In contrast, the number of tumors per mouse trended toward reduction in CXCR3-173–treated mice ($P = 0.0515$) (Supplemental Figure 5I), consistent with a role of CXCR3 in tumor initiation. Unfortunately, these data do not support a robust therapeutic effect for the tested CXCR3-173 dosing regimens.

Discussion

A variety of NF1 models have been developed to explore the effects of NF1 loss/Ras pathway hyperactivation on the development of plexiform neurofibroma (19, 26, 31, 33, 38, 39). Differences in the biology between models/strains with regard to the nature and timing of the inflammatory response and its contribution to neurofibroma development provided useful insights into the mechanisms of disease development. In this study, the comparison of 2 models with similar nerve pathology and modest differences in gene expression, but a different capacity to form tumors, led to the identification of a potentially novel signaling pathway, CXCL10/CXCR3, as a key contributor to neurofibroma development and the maintenance of macrophages in neurofibromas (Figure 6, A and B).

CXCR3 ligand production is frequently associated with a myeloid cell response to IFN-γ signaling (46, 47). IFN-γ is unlikely to drive *Cxcl10* expression in neurofibroma; however, because *Ifng* expression is not detectable early in neurofibroma formation, in 2-month *Dhh*-Cre *Nf1*$^{fl/fl}$ nerve/DRG, IFN-γ levels in neurofibroma are low relative to other relevant cytokines (17). Rather, it appears that SCs, like CNS glia, produce *Cxcl10* in an IFN-γ–independent fashion (47), because we found that *Cxcl10* expression in 2-month *Dhh*-Cre *Nf1*$^{fl/fl}$ nerve/DRG localized to cell clusters expressing SC-associated genes. This finding is consistent with prior work showing that transient Raf hyperactivation in SCs can induce *Cxcl10* expression (48, 49). Consistent with Raf/Ras/MEK/ERK pathway signaling contributing to *Cxcl10* expression in SCs, *Cxcl10* expression was negatively correlated with *Nf1* expression in the SC clusters and positively correlated with the expression of AP-1 transcription factors and of downstream targets induced by Ras signaling. Type I IFNs can also contribute to *Cxcl10* expression, and expression of type 1 IFN targets was also correlated with *Cxcl10* expression and may play a role in neurofibroma SCs.

Notably, *Cxcl10* expression in cluster C9 negatively correlated with *Nf1* expression and was positively correlated with *Fabp7* and other satellite glia/immature SC genes, suggesting that *Cxcl10* is expressed by satellite glia and/or by SCs that decrease expression of more mature markers. In contrast, expression of *Cxcl10* negatively correlated with expression of *Ngfr* and *Gap43*, markers that are associated with Remak SCs in vivo. In neurofibroma, when *Ngfr*-expressing SCs become axon dissociated, they secrete macrophage and mast cell chemokines (16, 17, 50–52) but not *Cxcl10*. These data suggest that distinct SC subsets in neurofibromas produce different chemokines that contribute to tumor formation.

Deletion of the *Cxcr3* receptor was sufficient to completely prevent neurofibroma development and to reduce nerve pathology in our NF1 mouse model. Because both mast cells and macrophages have been reported to express *Cxcr3* (42, 43, 53) and have been implicated in promoting nerve pathology and neurofibroma development (20, 22), we initially investigated the role of *Cxcr3* on these cell types. However, loss of *Cxcr3* did not affect the initial recruitment of these cells to inflamed nerves. Consistent with this finding, *Cxcr3* expression did not localize to these cell populations but instead to T cells (CD3$^+$) and DCs (CD11c$^+$). Interestingly, macrophage numbers were nonetheless reduced in the nerves of older (7-month) *Dhh*-Cre *Nf1*$^{fl/fl}$ *Cxcr3*-null mice. This suggests that progression to neurofibroma might be prevented by the absence of CXCR3 signaling to T cells and DCs, perhaps ultimately allowing for a resolution of nerve/

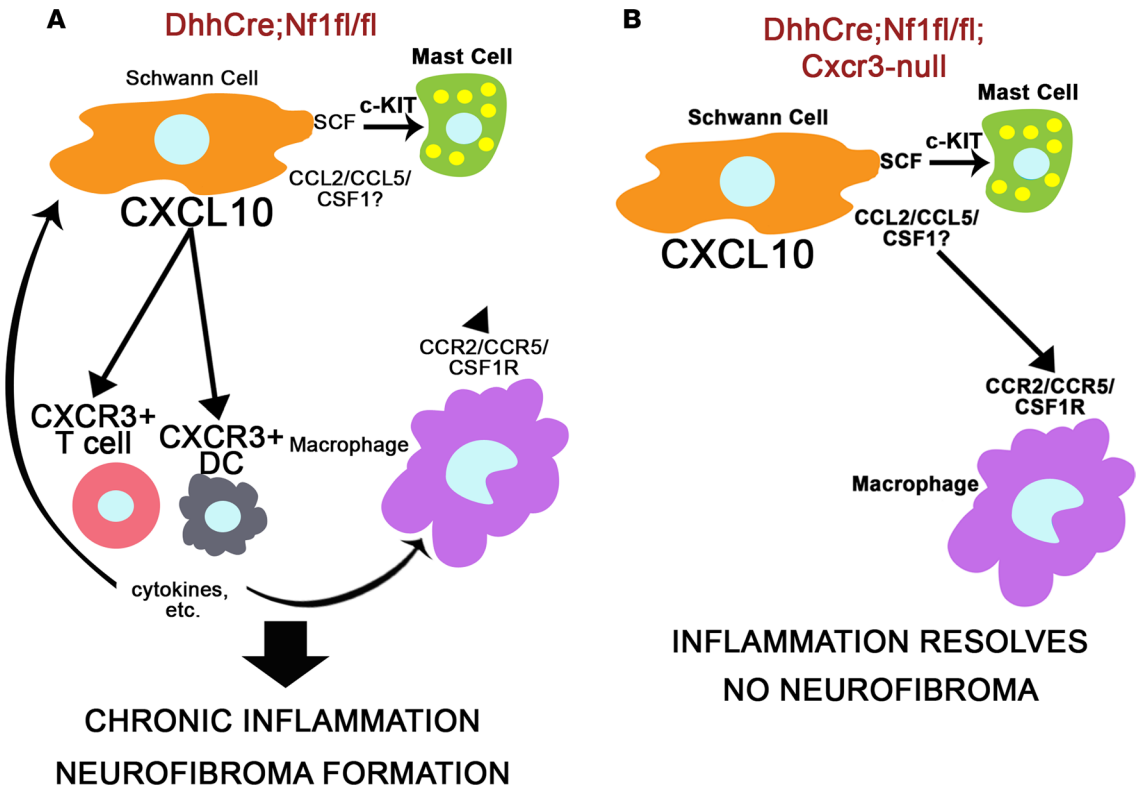

Figure 6. The proposed role of *Cxcr3*-expressing T cells and DCs in neurofibroma development. (**A**) In *Dhh*-Cre *Nf1*$^{fl/fl}$ DRG/nerve, SCs express chemokines and growth factors that can recruit macrophages, mast cells, and T cells/DCs. This likely drives the initial immune cell infiltration at the site of neurofibroma formation, consistent with our finding that loss of *Cxcr3* does not prevent macrophage or mast cell recruitment to 2-month *Dhh*-Cre *Nf1*$^{fl/fl}$ *Cxcr3*-null DRG/nerve. CXCR3 is predominantly expressed by T cells and DCs in *Dhh*-Cre *Nf1*$^{fl/fl}$ peripheral nerves and neurofibroma, and we hypothesize that cytokine production or other functions of T cells or DCs recruited through CXCR3 facilitate chronic inflammation and neurofibroma development. (**B**) Macrophage inflammation resolves by 7 months in *Dhh*-Cre *Nf1*$^{fl/fl}$ *Cxcr3*-null peripheral nerves, and neurofibromas do not form in these mice. We suggest that loss of *Cxcr3* reduces T cell and DC recruitment to these nerves, allowing for the resolution of nerve inflammation and the prevention of neurofibroma development.

DRG inflammation with age. Consistent with this hypothesis, GEMM-NF1–associated nerve pathology was reduced in the sciatic nerves of 7-month *Dhh*-Cre *Nf1*$^{fl/fl}$ *Cxcr3*-null mice.

T cells and DCs were exceedingly rare in normal nerve/DRG but increased in *Dhh*-Cre *Nf1*$^{fl/fl}$ DRG. In neurofibromas, intense focal accumulation of *Cxcr3*-expressing T cells and DCs was observed. We also demonstrated that both CD3$^+$ T cells and CD11c$^+$CD11b$^-$ DCs are present in mouse neurofibroma, and CD3$^+$ T cells and CD11c$^+$ cells, likely DCs, are present in human neurofibroma. The accumulation of these cells is pathological, because they were not detected in normal peripheral nerves. T cells have recently begun to be characterized as a component of human benign neurofibroma, but no work has been done to examine DCs as a distinct myeloid cell population in neurofibroma (54–56).

It is perhaps surprising to suggest that *Cxcr3*-expressing T cells and DCs contribute to neurofibroma development, because *Cxcr3* expression is frequently associated with an antitumor T cell response (57–60). However, cell death is rare in *Dhh*-Cre *Nf1*$^{fl/fl}$ DRG and neurofibroma (26), so it appears unlikely that these cells mediate significant levels of cytotoxic killing of neurofibroma SCs. *Cxcr3*-expressing T cells have been reported to facilitate protumorigenic inflammation in a mouse model of chemical skin carcinogenesis (61). Therefore, *Cxcr3*-expressing T cells may provide protumorigenic signals in a context- and dose-dependent fashion (62–64). Further studies are needed to better characterize the T cell and DC populations and functions in plexiform neurofibroma development and growth.

Unfortunately, treatment with the CXCR3-neutralizing antibody CXCR3-173 failed to reduce the tumor volume or the number of tumor T cells and DCs in established *Dhh*-Cre *Nf1*$^{fl/fl}$ neurofibroma. We hypothesized that this might be the result of a failure to block the initial recruitment of these cells to the nerve/DRG, because in a model of fetal tolerance, CXCR3 blockade with CXCR3-173 was able to prevent T cell recruitment, but not the cytokine production or cytotoxic activity of T cells already present in target tissue (46).

However, preventative treatment with CXCR3-173, initiated before significant T cell and DC recruitment to *Dhh*-Cre *Nf1*$^{fl/fl}$ nerve/DRG, also failed to prevent tumor development, even though the number of tumors per mouse showed a trend toward reduction (Supplemental Figure 5I). The antibody dosing regimen used was based on effective doses in a prior shorter-term study with a distinct context (65). In prostate cancer models, treatment of mice for 21 days with CXCR3-173 was also not effective in established disease (66). It may be that CXCR3 signaling is dispensable once T cells and DCs are established in tumors, that insufficient blockade of CXCR3 was achieved with treatment, or that other chemotactic signaling pathways can compensate for loss of CXCR3 signaling in T cell and DC recruitment to neurofibromas. Nonetheless, if future studies provide mechanistic support for a protumorigenic role of CXCR3 signaling in neurofibroma development, further exploration of CXCR3-targeted neurofibroma prophylaxis may be warranted. Small-molecule inhibitors of CXCR3 are an active area of drug development, with no serious adverse events reported in a phase I clinical trial of the CXCR3 inhibitor AMG-487 (67).

In summary, CXCR3 signaling is necessary for neurofibroma development in a mouse model of NF1, where it likely functions in the recruitment of T cells and DCs to inflamed nerves and neurofibroma. This study demonstrates that T cells and DCs are present in both human and mouse neurofibromas and that these cells may participate, directly or indirectly, in tumor initiation and in the processes of Remak bundle disruption, nerve fibrosis, and sustaining macrophage accumulation in neurofibromas. Future studies of GEMM-NF1 and human NF1 nerve and neurofibroma microenvironments should take into account the potential contributions of these cells to tumor development.

Methods

Mice. *Cxcr3*-deficient (B6.129P2-*Cxcr3*tm1Dgen/J, stock number 005772) and *Cxcr3* reporter (B6.129S4-*Cxcr3*tm1Arsa/SoghJ; stock no. 023337) mice on a C57BL/6 background were acquired from The Jackson Laboratory. These lines were crossed to an in-house *Dhh*-Cre *Nf1*$^{fl/fl}$ mouse line that had been previously backcrossed to C57BL/6 for more than 6 generations. Both male and female mice were used in experiments in roughly equivalent numbers. Tissues from mouse models used in the initial microarray analyses were acquired and processed as described previously (13).

Microarray analysis. The heatmap in Figure 1A represents a reanalysis of relevant mouse model samples from a microarray data set described previously (13). For the microarray analysis in Figure 1B, additional 1- and 2-month nerves from *Dhh*-Cre *Nf1*$^{fl/fl}$ and *CNPase*-hEGFR/*CNPase*-hEGFR mice, as well as *Nf1*$^{fl/fl}$ controls, were collected and analyzed using the same methods used for the original data set (13), and analysis data are available in Gene Expression Omnibus database (accession number GSE122999).

Real-time PCR. We isolated RNA with the RNeasy Plus Micro Kit for nerve/DRG and with QIAzol and RNeasy Mini Kit for neurofibroma per manufacturer's instructions (QIAGEN). cDNA was generated with a High Capacity cDNA Reverse Transcription Kit (Applied Biosystems). Real-time PCR was performed using the Power SYBR Green PCR Master Mix and primers for mouse *Gapdh*, *Cxcl9*, *Cxcl10*, *Cxcl11*, and *Cxcr3* (Supplemental Table 1). Relative quantification was calculated using average Ct values using the housekeeping gene GAPDH as an internal control.

scRNA-Seq. We dissociated 2-month *Dhh*-Cre *Nf1*$^{fl/fl}$ mouse DRG to obtain single cells as previously described (68, 69), with minor modifications. Specifically, DRG were cut into 1- to 2-mm^3 pieces and dissociated in 20 ml L-15 medium (Mediatech) containing 0.5 mg/ml collagenase type 1 (Worthington) and 2.5 mg/ml dispase protease type II (Cambrex) at 37°C for 2 hours. Then, 30 ml DMEM containing 10% FBS was added to stop the reaction. Cells were centrifuged and supernatant was removed. Next, cells were resuspended in 5 ml DMEM by trituration (×30) and filtered through 100-μm, 40-μm, and 20-μm cell strainers sequentially. After straining, cells were centrifuged and resuspended in 1× PBS containing 0.1% BSA at 1,000 cells/μl.

We then used the 10x Genomics Chromium instrument and cDNA synthesis kit to generate a barcoded cDNA library for scRNA-Seq from approximately 10,000 cells. cDNA library quality was determined using an Agilent Bioanalyzer. Using this library, we performed 1 full-lane sequence on 2 paired-end 75-bp flow cells using an Illumina HiSeq2500. We estimated that we would obtain 40 million to 300 million reads. The 10x Genomics Chromium single-cell RNA-Seq library was aligned to the mouse genome (mm10) using the Cell Ranger software package. Cell Ranger returned 1,820 expression-filtered barcodes with an average of 136,127 reads/barcode (median 13,568 unique molecular indices/barcode). These data are available in Gene Expression Omnibus database (accession number GSE122730).

The Cell Ranger–filtered sparse matrix files were processed in the software AltAnalyze to identify gene expression populations using the unsupervised subtype prediction software ICGS. ICGS identified 9 primary cell populations and associated population-specific genes following ICGS with the MarkerFinder analysis option (Supplemental Table 2).

To exclude potential multiplet cell profiles because of incomplete dissociation or multiplet cell droplets, we created a new function in the software AltAnalyze (removeDoublet) with a tunable parameter for more stringent hybrid profile removal. In brief, this script (https://github.com/nsalomonis/altanalyze/blob/master/stats_scripts/removeDoublets.py) collapses the median normalized expression of genes associated with each of the 9 identified cell clusters into 9 gene centroids from the ICGS MarkerFinder results. These cluster scores (CSs) are used for all downstream analyses. For each cell cluster, a reference CS profile is calculated based on the median CS for all cells in that cluster. This reference assumes the majority of cells in the cluster are not multiplets. If CS_w is the CS score for genes for the examined cell cluster (within) and CS_o is the maximum score in other cell clusters (outside), $CS_w - CS_o$ equals the specificity of gene expression of markers within that cell population relative to others (CS_{Diff}). If the CS_{Diff} of a cellular barcode is greater than the median reference CS_{Diff} for the same cluster and CS_{Diff} is greater than the user-supplied difference threshold (default = 1), the cellular barcode is considered a singlet profile and is retained. This conservative analysis reduced the scRNA-Seq data down from 1,800 cells to 662 cells that could not be associated with multiplets, including exclusion of cluster C8 as a putative doublet cluster. To assign higher-confidence cell-type assignments to these resultant clusters, we created a custom gene-to–cell type database for the software GO-Elite using markers previously reported for distinct immune, neural, and glial subsets (49, 70–72).

Tumor number and volume measurements. MRI data were collected on a 7-T Bruker BioSpec system equipped with 400G/cm gradients, and tumor burden was calculated as described previously (29). To quantify tumor numbers, we used a Leica dissecting microscope to dissect the spinal cord with attached DRG and nerve roots. A tumor was defined as a mass surrounding the DRG or nerve roots, with a diameter greater than 1 mm, measured perpendicular to DRG/nerve roots as described previously (69).

IHC and histology. For immunofluorescence staining, mice were perfused with chilled 0.1-M, 7.4-pH phosphate buffer, then perfusion fixed with chilled 4% paraformaldehyde in 1× PBS. Collected tissues were postfixed overnight at 4°C, then incubated overnight in 20% sucrose at 4°C before embedding in Neg 50 (Richard-Allan Scientific) for cryosectioning. Frozen sections (12 μm each) were blocked with 10% serum in 0.3% Triton-X in 1× PBS for 1 hour, labeled singly or multiply overnight at 4°C with primary antibodies against CD3 ([17A2], BioLegend), CD11c ([N418], Thermo Fisher Scientific), CD45 ([I3/2.3], Abcam), CXCL10 (AF-466-NA, R&D Systems; ab9938, Abcam), GFP, or Iba-1 (019-19741, Wako) in blocking solution. Primary antibody binding was visualized with appropriate combinations of fluorescently labeled secondary goat antibodies against rabbit (Alexa Fluor 488, A-11034, Invitrogen), rat (Alexa Fluor 555, A-21434, Invitrogen), or hamster (Alexa Fluor 647, 127-605-160, Jackson ImmunoResearch) for 1 hour. Cell nuclei were labeled with DAPI (0.1 μg/ml), and slides were mounted with cover glass using Fluoromount G (Electron Microscopy Sciences). Three 1× PBS rinses were performed between each step.

Mouse neurofibromas collected from 7-month CXCR3-173 study mice and human neurofibromas were formalin fixed, paraffin embedded, sectioned at 4-μm thickness, baked at 60°C for 1 hour, and air-dried. For staining, all sections were deparaffinized and rehydrated. For CD11c staining, antigen retrieval was performed by boiling slides for 10 minutes in 0.1 M citrate buffer at 6.0 pH. For CD3 staining, slides were boiled for 10 minutes in 0.1 M Tris-EDTA buffer (10 μM Tris base, 1 μM EDTA solution, 0.05% Tween 20, pH 8.5–9.0). After cooling, sections were rinsed with water and transferred to PBS. Endogenous peroxidase activity was quenched with 3% hydrogen peroxide for 10 minutes, and slides were blocked in 10% normal goat serum (Jackson ImmunoResearch) with 0.3% Triton-X-100 in 1× PBS for 1 hour. For CD11c staining, slides were incubated overnight at 4°C in primary antibody (ab52632, Abcam) diluted 1:1,000 in blocking solution. For CD3, sections were incubated in primary antibody (Ventana 790-4341; 1:1) for 15 minutes at 37°C and then for 15 minutes at room temperature (25°C). Sections for both CD11c and CD3 were then incubated in biotinylated goat anti–rabbit secondary antibody (Vector BA-1000) for 1 hour, rinsed in PBS 3 times for 5 minutes, incubated in avidin-biotin complex (ABC) (Vector PK-6100) for 1 hour, rinsed in PBS, incubated in DAB (Vector SK-4100) for 5 minutes, rinsed, dehydrated, and then mounted with Histomount (Life Technologies 008030).

Electron microscopy. Mice were perfusion fixed with 4% paraformaldehyde and 2.5% glutaraldehyde in 0.1-M phosphate buffer at 7.4 pH. Saphenous nerve was dissected out and postfixed overnight, then transferred to 0.175 mol/L cacodylate buffer, osmicated, dehydrated, and embedded in Embed 812

(Ladd Research Industries). Ultrathin sections were stained in uranyl acetate and lead citrate and viewed on a Hitachi H-7600 microscope.

Drug administration. *Dhh*-Cre *Nf1*$^{fl/fl}$ mice were treated with 200 μg hamster anti–CXCR3 neutralizing antibody (CXCR3-173, BioLegend) or hamster IgG control (BE0091, BioLegend) via intraperitoneal administration once daily, 3 days a week (Monday, Wednesday, Friday), based on prior treatment paradigms (45, 65).

Statistics. For microarray data analyses, ANOVA was used to identify differential gene expression between groups; all tests were corrected for multiple-testing effects by applying Benjamini-Hochberg FDR correction. For single-cell analysis, cell cluster–associated genes were identified using MarkerFinder (cell state–specific Pearson correlation coefficient > 0.3). Survival data were compared using the log-rank (Mantel-Cox) test. To test the effect of CXCR3-neutralizing antibody on established neurofibroma, a random-effects-model analysis on the log-transformed tumor volume data was performed as described previously (29). Other data were compared by 2-tailed Student's *t* test, 1-way ANOVA, or 2-way ANOVA as appropriate, with the differences between individual groups in ANOVA analyses being tested using Tukey's or Dunnett's MCT as indicated. A P value of < 0.05 was considered significant. These data are presented as the mean ±SD of more than 3 independent experiments. Data graphing and analyses were performed using GraphPad Prism 7.

Study approval. The animal care and use committees of Cincinnati Children's Hospital Medical Center approved all animal care and procedures. Human paraffin-embedded tissues were collected under Cincinnati Children's Hospital Medical Center IRB approval; the study qualified for exempt review.

Author contributions

JSF, JW, WJJ, and NR designed the studies. JSF, JP, JW, WJJ, JAM, and TAR conducted the experiments. JSF, JP, JW, WJJ, JAM, ED, MOK, TAR, KC, and NS analyzed the data. JSF, JW, NS, and NR wrote the manuscript.

Acknowledgments

We thank Lindsey Aschbacher-Smith and Joshua Pressler for technical support with drug administration and R. Scott Dunn for MRI. We also thank Steven Potter for assistance with single-cell isolation and library preparation. This work was supported by NIH R01 NS28840, Children's Tumor Foundation, Neurofibromatosis Therapeutic Acceleration Program, and Department of Defense W81XWH-11-1-0057 (to NR) and NIH F30 NS096796-02 (to JSF).

Address correspondence to: Nancy Ratner, Cincinnati Children's Hospital Medical Center, 3333 Burnet Ave., Cincinnati, Ohio 45229-0713, USA. Phone: 513.636.9469; Email: Nancy.Ratner@cchmc.org.

1. Prada CE, et al. Pediatric plexiform neurofibromas: impact on morbidity and mortality in neurofibromatosis type 1. *J Pediatr*. 2012;160(3):461–467.
2. Ferner RE, et al. Guidelines for the diagnosis and management of individuals with neurofibromatosis 1. *J Med Genet*. 2007;44(2):81–88.
3. Ferner RE, Gutmann DH. Neurofibromatosis type 1 (NF1): diagnosis and management. *Handb Clin Neurol*. 2013;115:939–955.
4. Plotkin SR, et al. Quantitative assessment of whole-body tumor burden in adult patients with neurofibromatosis. *PLoS One*. 2012;7(4):e35711.
5. Storlazzi CT, Von Steyern FV, Domanski HA, Mandahl N, Mertens F. Biallelic somatic inactivation of the NF1 gene through chromosomal translocations in a sporadic neurofibroma. *Int J Cancer*. 2005;117(6):1055–1057.
6. Beert E, et al. Biallelic inactivation of NF1 in a sporadic plexiform neurofibroma. *Genes Chromosomes Cancer*. 2012;51(9):852–857.
7. Pemov A, et al. The primacy of NF1 loss as the driver of tumorigenesis in neurofibromatosis type 1-associated plexiform neurofibromas. *Oncogene*. 2017;36(22):3168–3177.
8. Ohba Y, et al. Regulatory proteins of R-Ras, TC21/R-Ras2, and M-Ras/R-Ras3. *J Biol Chem*. 2000;275(26):20020–20026.
9. Donovan S, Shannon KM, Bollag G. GTPase activating proteins: critical regulators of intracellular signaling. *Biochim Biophys Acta*. 2002;1602(1):23–45.
10. Maertens O, Cichowski K. An expanding role for RAS GTPase activating proteins (RAS GAPs) in cancer. *Adv Biol Regul*. 2014;55:1–14.
11. Kim HA, Rosenbaum T, Marchionni MA, Ratner N, DeClue JE. Schwann cells from neurofibromin deficient mice exhibit activation of p21ras, inhibition of cell proliferation and morphological changes. *Oncogene*. 1995;11(2):325–335.
12. Sherman LS, Atit R, Rosenbaum T, Cox AD, Ratner N. Single cell Ras-GTP analysis reveals altered Ras activity in a subpopulation of neurofibroma Schwann cells but not fibroblasts. *J Biol Chem*. 2000;275(39):30740–30745.
13. Jessen WJ, et al. MEK inhibition exhibits efficacy in human and mouse neurofibromatosis tumors. *J Clin Invest*. 2013;123(1):340–347.
14. Brundage ME, et al. MAF mediates crosstalk between Ras-MAPK and mTOR signaling in NF1. *Oncogene*. 2014;33(49):5626–5636.

15. Patmore DM, et al. In vivo regulation of TGF-β by R-Ras2 revealed through loss of the RasGAP protein NF1. *Cancer Res*. 2012;72(20):5317–5327.
16. Ryan JJ, et al. Role for the stem cell factor/KIT complex in Schwann cell neoplasia and mast cell proliferation associated with neurofibromatosis. *J Neurosci Res*. 1994;37(3):415–432.
17. Choi K, et al. An inflammatory gene signature distinguishes neurofibroma Schwann cells and macrophages from cells in the normal peripheral nervous system. *Sci Rep*. 2017;7:43315.
18. Courtois-Cox S, et al. A negative feedback signaling network underlies oncogene-induced senescence. *Cancer Cell*. 2006;10(6):459–472.
19. Yang FC, et al. Nf1-dependent tumors require a microenvironment containing $Nf1^{+/-}$ and c-kit-dependent bone marrow. *Cell*. 2008;135(3):437–448.
20. Prada CE, et al. Neurofibroma-associated macrophages play roles in tumor growth and response to pharmacological inhibition. *Acta Neuropathol*. 2013;125(1):159–168.
21. Robertson KA, et al. Imatinib mesylate for plexiform neurofibromas in patients with neurofibromatosis type 1: a phase 2 trial. *Lancet Oncol*. 2012;13(12):1218–1224.
22. Staser K, Yang FC, Clapp DW. Mast cells and the neurofibroma microenvironment. *Blood*. 2010;116(2):157–164.
23. Varricchi G, et al. Are mast cells MASTers in cancer? *Front Immunol*. 2017;8:424.
24. Murray PJ. Nonresolving macrophage-mediated inflammation in malignancy. *FEBS J*. 2018;285(4):641–653.
25. Schupp J, Krebs FK, Zimmer N, Schuppan D, Trzeciak E, Tuettenberg A. Targeting myeloid cells in the tumor sustaining microenvironment. [published online ahead of print November 1, 2017]. *Cell Immunol*. https://doi.org/10.1016/j.cellimm.2017.10.013.
26. Wu J, et al. Plexiform and dermal neurofibromas and pigmentation are caused by Nf1 loss in desert hedgehog-expressing cells. *Cancer Cell*. 2008;13(2):105–116.
27. Jousma E, et al. Preclinical assessments of the MEK inhibitor PD-0325901 in a mouse model of Neurofibromatosis type 1. *Pediatr Blood Cancer*. 2015;62(10):1709–1716.
28. Miller SJ, et al. Integrative genomic analyses of neurofibromatosis tumours identify SOX9 as a biomarker and survival gene. *EMBO Mol Med*. 2009;1(4):236–248.
29. Wu J, et al. Preclincial testing of sorafenib and RAD001 in the Nf(flox/flox) ;DhhCre mouse model of plexiform neurofibroma using magnetic resonance imaging. *Pediatr Blood Cancer*. 2012;58(2):173–180.
30. Mayes DA, et al. Perinatal or adult Nf1 inactivation using tamoxifen-inducible PlpCre each cause neurofibroma formation. *Cancer Res*. 2011;71(13):4675–4685.
31. Zheng H, et al. Induction of abnormal proliferation by nonmyelinating schwann cells triggers neurofibroma formation. *Cancer Cell*. 2008;13(2):117–128.
32. Le LQ, Liu C, Shipman T, Chen Z, Suter U, Parada LF. Susceptible stages in Schwann cells for NF1-associated plexiform neurofibroma development. *Cancer Res*. 2011;71(13):4686–4695.
33. Ling BC, et al. Role for the epidermal growth factor receptor in neurofibromatosis-related peripheral nerve tumorigenesis. *Cancer Cell*. 2005;7(1):65–75.
34. Billottet C, Quemener C, Bikfalvi A. CXCR3, a double-edged sword in tumor progression and angiogenesis. *Biochim Biophys Acta*. 2013;1836(2):287–295.
35. Van Raemdonck K, Van den Steen PE, Liekens S, Van Damme J, Struyf S. CXCR3 ligands in disease and therapy. *Cytokine Growth Factor Rev*. 2015;26(3):311–327.
36. Müller M, Carter S, Hofer MJ, Campbell IL. Review: The chemokine receptor CXCR3 and its ligands CXCL9, CXCL10 and CXCL11 in neuroimmunity — a tale of conflict and conundrum. *Neuropathol Appl Neurobiol*. 2010;36(5):368–387.
37. Monk KR, et al. Mast cells can contribute to axon-glial dissociation and fibrosis in peripheral nerve. *Neuron Glia Biol*. 2007;3(3):233–244.
38. Vogel KS, Klesse LJ, Velasco-Miguel S, Meyers K, Rushing EJ, Parada LF. Mouse tumor model for neurofibromatosis type 1. *Science*. 1999;286(5447):2176–2179.
39. Patel AV, et al. Ras-driven transcriptome analysis identifies aurora kinase A as a potential malignant peripheral nerve sheath tumor therapeutic target. *Clin Cancer Res*. 2012;18(18):5020–5030.
40. Rhode A, et al. Islet-specific expression of CXCL10 causes spontaneous islet infiltration and accelerates diabetes development. *J Immunol*. 2005;175(6):3516–3524.
41. Groom JR, Luster AD. CXCR3 ligands: redundant, collaborative and antagonistic functions. *Immunol Cell Biol*. 2011;89(2):207–215.
42. Wenzel J, Tüting T. An IFN-associated cytotoxic cellular immune response against viral, self-, or tumor antigens is a common pathogenetic feature in "interface dermatitis". *J Invest Dermatol*. 2008;128(10):2392–2402.
43. Brightling CE, et al. The CXCL10/CXCR3 axis mediates human lung mast cell migration to asthmatic airway smooth muscle. *Am J Respir Crit Care Med*. 2005;171(10):1103–1108.
44. Oghumu S, et al. Distinct populations of innate CD8+ T cells revealed in a CXCR3 reporter mouse. *J Immunol*. 2013;190(5):2229–2240.
45. Uppaluri R, et al. Prolongation of cardiac and islet allograft survival by a blocking hamster anti-mouse CXCR3 monoclonal antibody. *Transplantation*. 2008;86(1):137–147.
46. Chaturvedi V, et al. CXCR3 blockade protects against Listeria monocytogenes infection-induced fetal wastage. *J Clin Invest*. 2015;125(4):1713–1725.
47. Lin AA, Tripathi PK, Sholl A, Jordan MB, Hildeman DA. Gamma interferon signaling in macrophage lineage cells regulates central nervous system inflammation and chemokine production. *J Virol*. 2009;83(17):8604–8615.
48. Ribeiro S, et al. Injury signals cooperate with Nf1 loss to relieve the tumor-suppressive environment of adult peripheral nerve. *Cell Rep*. 2013;5(1):126–136.
49. Balakrishnan A, Stykel MG, Touahri Y, Stratton JA, Biernaskie J, Schuurmans C. Temporal analysis of gene expression in the murine schwann cell lineage and the acutely injured postnatal nerve. *PLoS One*. 2016;11(4):e0153256.
50. Perrin GQ, et al. Plexiform-like neurofibromas develop in the mouse by intraneural xenograft of an NF1 tumor-derived

Schwann cell line. *J Neurosci Res*. 2007;85(6):1347–1357.
51. Wu J, et al. Perinatal epidermal growth factor receptor blockade prevents peripheral nerve disruption in a mouse model reminiscent of benign world health organization grade I neurofibroma. *Am J Pathol*. 2006;168(5):1686–1696.
52. Yang FC, et al. Neurofibromin-deficient Schwann cells secrete a potent migratory stimulus for Nf1+/- mast cells. *J Clin Invest*. 2003;112(12):1851–1861.
53. van Zwam M, Wierenga-Wolf AF, Melief MJ, Schrijver B, Laman JD, Boven LA. Myelin ingestion by macrophages promotes their motility and capacity to recruit myeloid cells. *J Neuroimmunol*. 2010;225(1-2):112–117.
54. Farschtschi S, et al. Effector T cell subclasses associate with tumor burden in neurofibromatosis type 1 patients. *Cancer Immunol Immunother*. 2016;65(9):1113–1121.
55. Haworth KB, et al. Immune profiling of NF1-associated tumors reveals histologic subtype distinctions and heterogeneity: implications for immunotherapy. *Oncotarget*. 2017;8(47):82037–82048.
56. Wang S, et al. Programmed death ligand 1 expression and tumor infiltrating lymphocytes in neurofibromatosis type 1 and 2 associated tumors. *J Neurooncol*. 2018;138(1):183–190.
57. Li J, et al. IFNγ-induced Chemokines Are Required for CXCR3-mediated T-Cell Recruitment and Antitumor Efficacy of Anti-HER2/CD3 Bispecific Antibody. *Clin Cancer Res*. 2018;24(24):6447–6458.
58. Chheda ZS, Sharma RK, Jala VR, Luster AD, Haribabu B. Chemoattractant receptors BLT1 and CXCR3 regulate antitumor immunity by facilitating $CD8^+$ T cell migration into tumors. *J Immunol*. 2016;197(5):2016–2026.
59. Hensbergen PJ, Wijnands PG, Schreurs MW, Scheper RJ, Willemze R, Tensen CP. The CXCR3 targeting chemokine CXCL11 has potent antitumor activity in vivo involving attraction of CD8+ T lymphocytes but not inhibition of angiogenesis. *J Immunother*. 2005;28(4):343–351.
60. Mikucki ME, et al. Non-redundant requirement for CXCR3 signalling during tumoricidal T-cell trafficking across tumour vascular checkpoints. *Nat Commun*. 2015;6:7458.
61. Winkler AE, et al. CXCR3 enhances a T-cell-dependent epidermal proliferative response and promotes skin tumorigenesis. *Cancer Res*. 2011;71(17):5707–5716.
62. Zaidi MR, Merlino G. The two faces of interferon-γ in cancer. *Clin Cancer Res*. 2011;17(19):6118–6124.
63. Murugaiyan G, Saha B. Protumor vs antitumor functions of IL-17. *J Immunol*. 2009;183(7):4169–4175.
64. Yoshimura A. Signal transduction of inflammatory cytokines and tumor development. *Cancer Sci*. 2006;97(6):439–447.
65. Dai Z, et al. CXCR3 Blockade Inhibits T Cell Migration into the Skin and Prevents Development of Alopecia Areata. *J Immunol*. 2016;197(4):1089–1099.
66. Li J, et al. Tumor cell-intrinsic factors underlie heterogeneity of immune cell infiltration and response to immunotherapy. *Immunity*. 2018;49(1):178–193.e7.
67. Andrews SP, Cox RJ. Small molecule CXCR3 antagonists. *J Med Chem*. 2016;59(7):2894–2917.
68. Wu J, Liu W, Williams JP, Ratner N. EGFR-Stat3 signalling in nerve glial cells modifies neurofibroma initiation. *Oncogene*. 2017;36(12):1669–1677.
69. Wu J, et al. Insertional mutagenesis identifies a STAT3/Arid1b/β-catenin pathway driving neurofibroma initiation. *Cell Rep*. 2016;14(8):1979–1990.
70. Li CL, et al. Somatosensory neuron types identified by high-coverage single-cell RNA-sequencing and functional heterogeneity. *Cell Res*. 2016;26(1):83–102.
71. Li C, Wang S, Chen Y, Zhang X. Somatosensory neuron typing with high-coverage single-cell RNA sequencing and functional analysis. *Neurosci Bull*. 2018;34(1):200–207.
72. Heng TS, Painter MW, Immunological Genome Project Consortium. The Immunological Genome Project: networks of gene expression in immune cells. *Nat Immunol*. 2008;9(10):1091–1094.